https://doi.org/10.1016/j.jsv.2023.117729

Vibration Characteristics and Cross-feedback Control of Magnetically Suspended Blower Based on Complex-factor Model

Biao Xiang[1], Jianmin Xu[1], Zhikai Liu[1], Waion Wong[2] and Lingbo Zheng[3]

1, School of Mechano-Electronic Engineering, Xidian University, Xi'an 710071, China
2, Department of Mechanical Engineering, Hongkong Polytechnic University, Kowloon, Hongkong, China
3, Department of Aerospace Science and Technology, Space Engineering University, Beijing 101416, China

***Abstract*—The research of vibration characteristics and active control methods of the magnetically suspended blower (MSB) are conducted for mitigation of the vibration amplitudes and the dynamic displacements of rotor shaft of the MSB at high speed. Firstly, the dynamic models with four degrees of freedom (DOFs) of the rotor shaft in the MSB are established. Secondly, the vibration characteristics of rotor shaft considering the rotor unbalance and misalignment are analyzed using the complex-factor model. Furthermore, the complex-factor and complex-exponential function cross-feedback models are respectively used to suppress the vibration amplitudes and the dynamic displacements of rotor shaft. Both numerical simulation and experimental tests of the cross-feedback model are conducted to verify the models. It is shown that a wide cutoff frequency of low-pass filter (LPF) could mitigate the precession, and a wide cutoff frequency of high-pass filter (HPF) could suppress the nutation. The proposed complex-exponential function cross-feedback model could be used to reduce the precession amplitude of the rotor shaft by 38.88%, and mitigate its nutation by 60.42%.**

***Index Terms*—magnetically suspended blower, active control, vibration characteristics, rotor unbalance, cross-feedback model**

1 Introduction

High speed rotational machine can easily suffered from vibrations due to mass eccentricity of its rotor or external disturbance leading to problems of dynamic stability and operational accuracy of the machine [1]. Therefore, the researches about the vibration analysis and the control methods of the high speed machinery are critical to ensure the dynamic and control stability of the machinery [2]. The rotor of the traditional rotational machines is supported by mechanical bearings and gears. The contact support would transfer any external vibration from the stator to the rotor shaft [3]. Moreover, the friction between the stator and the rotor shaft would also limit rotating speed [4] of the traditional rotational machinery with mechanical bearings and gears. On the other hand, the active magnetic bearing (AMB) has the benefits on contactless support and convenient active vibration control, no lubrication requirement, etc. [5, 6]. The AMB is therefore more suitable to be used in high speed rotational machine than the mechanical bearing. For example, in the control moment gyro [7, 8] and momentum flywheel [9, 10] of satellites, the AMB is used to eliminate the fiction between the stator and the rotor, and active control technology could be applied to improve the precision of generated moment. Moreover, in the flywheel energy storage system (FESS), the AMB is applied to levitate the heavy flywheel rotor so that the power storage of FESS with great momentum and high rotating speed can be improved [11, 12].

The blower needs to work at a higher rotating speed to improve its working efficiency. Any friction between the rotor and stator of the blower should be mitigated to extend its service life. The AMB is therefore a good choice of bearing to provide the suspension with five degrees of freedom (DOFs) and active control of the rotor shaft and impeller of the blower. However, the vibration displacements caused by the unbalance terms due to manufacturing or misalignment of the rotor can affect the suspension stability of the magnetically suspended blower (MSB) [13, 14]. In view of the above-mentioned reasons, the vibration characteristics and active control methods of the MSB are worthy of detailed investigations such that effective vibration control methods can be applied for mitigation of the rotor vibrations of the high-speed blower.

Xiang and Wong [15] studied the vibration behavior of rotor shaft in the magnetically suspended FESS by analyzing the stiffness and damping characteristics. The analysis results showed that the great damping coefficient could suppress the displacement deflections of rotor shaft in the magnetically suspended FESS as a passive means. However, too high the damping in the flywheel rotor would slow down its response rate to the control signal. The whirling-vibration performances of magnetically suspended rotor at different rotating speeds were reported by Kandil [16]. The nonlinear-vibration characteristics of magnetically suspended rotor were analyzed by numerical simulation of the whirl orbit without any experimental validation. The dynamics analysis of the magnetically suspended rotor with misalignment was reported by Kuppa and Lal [17]. The gyroscopic high-frequency condensation is found better than the standard high-frequency condensation for suppressing excessive vibration of the rotor. Tiwari and Kumar [18] considered any misalignment of the flexible rotor suspended by the AMB system, the vibration behavior and the model-based identification were realized by a virtual trial misalignment model. The suspension stability on four DOFs of magnetically suspended rotor with time delay was analyzed by Soni et al. [19]. Both numerical simulation and experimental results showed that the analysis method based on the system poles could be effective for the proof of system stability, but the nutation vibration at high rotating speed was not considered in the analysis. Ebrahimi et al. [20] analyzed the chaotic vibration of a coaxial rotor suspended by the AMB. The analysis results showed that the rotating speed had significant effect on the dynamic responses of the rotor shaft, but no vibration control model was proposed to mitigate the chaotic vibration.

Based on the researches about vibration characteristics of magnetically suspended rotor shaft, active control methods [21, 22] were proposed to mitigate the displacement deflections and vibration amplitudes. The vibration dynamics of rotor shaft supported with active magnetic bearings were analyzed by Cole and Fakkaew [23]. A decoupling model was proposed to mitigate the coupling dynamics of rotor shaft by Numanoy and Srisertpol [24]. In general, the cross-feedback control model could be designed to suppress the gyroscopic effect of the magnetically suspended rotor [25, 26], and the results indicate that the steady state dynamic displacement of the magnetically suspended rotor has only small fluctuation. However, the rotating speed of the magnetically suspended rotor in above-mentioned paper is limited. Moreover, notch filter [27] was also used to suppress the harmonic vibration of magnetically suspended rotor. Test results indicated that the amplitude of resonant vibration was significantly mitigated, but nutation vibration was not analyzed and suppressed. The adaptive frequency estimation method [28] was proposed for the suppression of synchronous vibration of magnetically suspended rotor. For a bearingless motor system, a novel vibration control method using the *d*-axis current was proposed to

suppress the axial vibration at the critical speed [29]. However, the complicated radial vibration of bearingless motor was not controlled. A fuzzy robust control diagram [30] was also proposed to suppress the vibration amplitude of magnetically suspended rotor, and the suspension robustness was improved.

Above all, the researches about the magnetically suspended rotor shaft found in literatures were focused on analyzing the synchronous vibration, and active control methods were proposed to control the synchronous and harmonic vibrations of the rotor shaft. However, the vibration characteristics of rotor shaft in the MSB due to unbalance terms are not researched, and the active control methods proposed in relevant literatures are too complicated to be applied to industrial products. Compared to the normal complex-factor cross feedback control model, the proposed complex-exponential function cross-feedback control model using the high-frequency and low-frequency pass filter is proved to be more useful of suppressing the vibration of the magnetically suspended blower at high rotating speed. The contributions of this research are listed as follows.

(1) A novel analysis method based on the complex-factor model is proposed to analyze the vibration characteristics of the MSB due to the unbalance terms, and the precise vibration models are established.

(2) A cross-feedback control model using the complex-exponential function method is proposed to effectively control the low-frequency precession and the high-frequency nutation of the MSB.

In this article, the vibration model of rotor shaft in the MSB is developed in Section 2. The active vibration control models of rotor shaft based on the cross-factor and the complex-exponential function cross-feedback model are designed in Section 3. Furthermore, simulations of the vibration characteristics and cross-feedback model are presented in Section 4. Experiments are conducted to analyze the control performances of the proposed control model and reported in Section 5. Finally, conclusions are drawn in Section 6.

2 Vibration Modelling of Rotor Shaft in MSB

2.1 Structure of MSB

As shown in Fig. 1, the MSB includes one pair of axial AMB unit, two pairs of radial AMB units, two protective bearings, axial/radial displacement sensors and a permanent magnet synchronous motor (PMSM). Specifically, the thrust AMB unit could generate the magnetic force to lift and suspend the rotor shaft at the equilibrium position along the axial axis. The mechanical friction between the stator and the rotor shaft is therefore eliminated. The two pairs of radial AMB units at the lower and upper ends could generate magnetic forces to stably suspend the rotor shaft at the equilibrium position along the radial direction. The tilting torques generated by two pairs of radial AMB units at the lower and upper ends of stator would also suppress the torsions of rotor shaft about the radial axes. Moreover, two protective bearings with 0.5 mm protective airgap at the lower and upper ends could restrain the excessive vibration displacements of rotor shaft when the AMB units have bearing failures in radial and axial directions. The eddy current displacement sensors mounted at the lower and upper ends of stator could timely detect the dynamic displacements of rotor shaft in radial axes, and the eddy current displacement sensor below the thrust disc could measure the dynamic displacements of rotor shaft in axial axis. Therefore, based on the displacement feedback in radial and axial axes, the five-DOFs closed-loop active control and stable suspension of rotor shaft in the MSB are realized. When the rotor shaft is stably suspended at the

equilibrium positions by the radial/axial AMB units, the PMSM could be used to regulate the rotational speed of rotor shaft according to different operational commands.

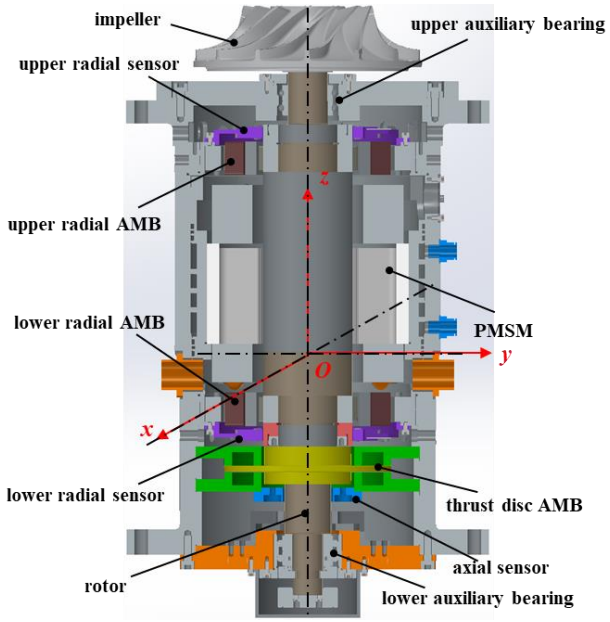

Fig. 1. The prototype and structure of the MSB.

2.2 Dynamic Models of Rotor Shaft in MSB

As shown in Fig. 2(a), the magnetic forces $\boldsymbol{f}_a=[f_{xu}, f_{yu}, f_{xl}, f_{yl}]$ generated by the upper-end and lower-end radial AMB units control the four DOFs motions of rotor shaft including the radial suspension and the tilting motion. The suspension span from the upper-end radial AMB unit to the mass of center of rotor shaft is defined as l_a, and the measurement span from the radial eddy current displacement sensor to the mass of center of rotor shaft is l_s. The generalized four-DOFs displacement variables of the rotor shaft are defined as $\boldsymbol{d}=[x, \beta, y, -\alpha]^{\mathrm{T}}$, and the inertial four-DOFs displacement variables of rotor shaft are chosen as $\boldsymbol{d}_i=[x_i, \beta_i, y_i, -\alpha_i]^{\mathrm{T}}$. The dynamic models of the rotor shaft on four DOFs are expressed as

$$\begin{cases} m\ddot{x}_i = f_{xu} + f_{xl} \\ J_e\ddot{\beta}_i - J_p\Omega\dot{\alpha}_i = p_\beta = f_{xl}l_a - f_{xu}l_a \\ m\ddot{y}_i = f_{yu} + f_{yl} \\ J_e\ddot{\alpha}_i + J_p\Omega\dot{\beta}_i = p_\alpha = f_{yu}l_a - f_{yl}l_a \end{cases} \tag{1}$$

where m is the mass of rotor shaft. J_e is the equatorial momentum of inertial, and J_p is the polar momentum of inertial.

The dynamic model in Eq. (1) could be written in matrix form as

$$\boldsymbol{M}\ddot{\boldsymbol{d}}_i + \boldsymbol{G}\dot{\boldsymbol{d}}_i = \boldsymbol{f} \tag{2}$$

where $\boldsymbol{M}$=diag[m, J_e, m, J_e] is the mass matrix of the rotor shaft. $\boldsymbol{G} = \begin{bmatrix} 0 & 0 & 0 & 0 \\ 0 & 0 & 0 & J_p\Omega \\ 0 & 0 & 0 & 0 \\ 0 & -J_p\Omega & 0 & 0 \end{bmatrix}$ is the coupling matrix on four DOFs, and $\boldsymbol{f} = \boldsymbol{T}_f \boldsymbol{f}_a = \begin{bmatrix} 1 & 1 & 0 & 0 \\ l_a & -l_a & 0 & 0 \\ 0 & 0 & 1 & 1 \\ 0 & 0 & -l_a & l_a \end{bmatrix} \begin{bmatrix} f_{xl} \\ f_{xu} \\ f_{yl} \\ f_{yu} \end{bmatrix}$ is the force/torque matrix generated by the radial AMB.

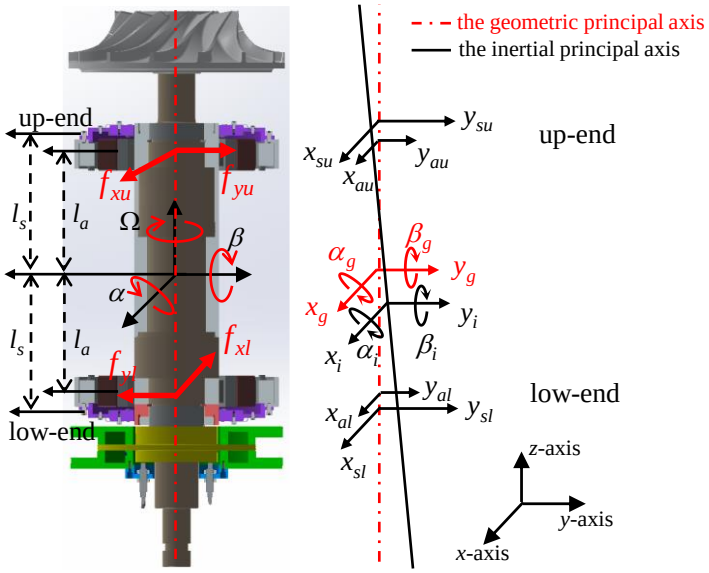

(a) (b)

Fig. 2. The force analysis and coordinate definition of the rotor shaft on four DOFs, (a) the force model of rotor shaft in the MSB, (b) the geometrical coordinates of the rotor shaft in the MSB.

The magnetic forces of the radial AMB units of four DOFs could be expressed as a linear function with the current stiffness k_i and the displacement stiffness k_d as

$$\boldsymbol{f}_a = k_i \boldsymbol{i}_a + k_d \boldsymbol{d}_a \tag{3}$$

where the control currents of radial AMB units are $\boldsymbol{i}_a$=[i_{xu}, i_{xl}, i_{yu}, i_{yl}].

The geometrical coordinates of rotor shaft and radial AMB units in the MSB are illustrated in Fig. 2(b). The red dashed line shows the geometrical principal axis of the rotor shaft, and the black solid line illustrates the inertial principal axis. The displacement variables of the radial AMB units are $\boldsymbol{d}_a$=[x_{au}, x_{al}, y_{au}, y_{al}]$^{\mathrm{T}}$, and the radial displacement variables measured by the displacement sensors are $\boldsymbol{d}_s$=[x_{su}, x_{sl}, y_{su}, y_{sl}]$^{\mathrm{T}}$. As illustrated in Fig. 2(b), the four-DOFs displacement terms of the rotor shaft varying with the inertial principal axis are defined as $\boldsymbol{d}_i$=[x_i, β_i, y_i, -α_i]$^{\mathrm{T}}$ with subscript 'i', and the four-DOFs displacement terms of the rotor shaft varying with the geometrical principal axis are $\boldsymbol{d}_g$=[x_g, β_g, y_g, -α_g]$^{\mathrm{T}}$ with subscript 'g'. Furthermore, the coordinate transfer function from the displacement coordinate of rotor shaft to that of the radial AMB units of four-DOFs is expressed as

$$\boldsymbol{d}_a = \boldsymbol{T}_f^T \boldsymbol{d}_g, \text{with } \boldsymbol{T}_f = \begin{bmatrix} 1 & 1 & 0 & 0 \\ l_a & -l_a & 0 & 0 \\ 0 & 0 & 1 & 1 \\ 0 & 0 & -l_a & l_a \end{bmatrix} \tag{4}$$

The coordinate transfer function from the displacement coordinate of rotor shaft to that of radial displacement sensors of four-DOFs is

$$\boldsymbol{d}_s = \boldsymbol{T}_s \boldsymbol{d}_g, \text{with } \boldsymbol{T}_s = k_s \begin{bmatrix} 1 & l_s & 0 & 0 \\ 1 & -l_s & 0 & 0 \\ 0 & 0 & 1 & l_s \\ 0 & 0 & 0 & -l_s \end{bmatrix} \tag{5}$$

where k_s is the measurement sensitivity of the radial eddy current displacement sensor.

In the practical control of the rotor shaft in the MSB, the reference displacements of the rotor shaft with four-DOFs are defined as $\boldsymbol{d}_{ref}$=[0, 0, 0, 0]$^{\mathrm{T}}$. The control currents of the radial AMB units using the control function $\boldsymbol{G}_c(s)$ and the power amplification function $\boldsymbol{G}_a(s)$ could be expressed as

$$\boldsymbol{i}_a = \left[\boldsymbol{d}_{ref} - \boldsymbol{d}_s\right] \boldsymbol{G}_c(s) \boldsymbol{G}_a(s) \tag{6}$$

The force model of the radial AMB unit in Eq. (3) is rewritten as

$$\boldsymbol{f}_a = k_i \boldsymbol{G}_c(s) \boldsymbol{G}_a(s) \left[\boldsymbol{d}_{ref} - \boldsymbol{d}_s\right] + k_d \boldsymbol{d}_a \tag{7}$$

Substituting Eqs. (3), (4) and (5) into Eq. (2), the dynamic models of the rotor shaft could be obtained as

$$\boldsymbol{M}\ddot{\boldsymbol{d}}_i + \boldsymbol{G}\dot{\boldsymbol{d}}_i = \boldsymbol{T}_f \left[k_i \boldsymbol{G}_c(s) \boldsymbol{G}_a(s) \left(-\boldsymbol{T}_s \boldsymbol{d}_g\right) + k_d \boldsymbol{T}_f^T \boldsymbol{d}_g \right] \tag{8}$$

The control function $\boldsymbol{G}_c(s)$ of the radial AMB unit is written as

$$\boldsymbol{G}_c(s) = \boldsymbol{T}_s \boldsymbol{G}_s(s) \boldsymbol{T}_s^{-1} \tag{9}$$

The reference control currents $\boldsymbol{i}_{ref}$=[i_{rax}, i_{rbx}, i_{ray}, i_{rby}]$^{\mathrm{T}}$ are expressed as

$$\boldsymbol{i}_{ref}(s) = \boldsymbol{G}_c(s) \left[-\boldsymbol{T}_s \boldsymbol{d}_g(s)\right] \tag{10}$$

The control current $\boldsymbol{i}_a$ of the radial AMB units through the power amplification unit $\boldsymbol{G}_a(s)$ in Fig. 3 could be derived as

$$\begin{aligned} \boldsymbol{i}_a(s) &= \boldsymbol{G}_{a1}(s) \boldsymbol{i}_{ref}(s) + \boldsymbol{G}_{a2}(s) \boldsymbol{d}_a(s) \\ &= \frac{k_a k_v}{R_a + k_a k_v k_c k_e} \frac{\omega_a}{s + \omega_a} \boldsymbol{i}_{ref}(s) - \frac{k_i}{k_a k_v} \frac{k_a k_v}{R_a + k_a k_v k_c k_e} \frac{\omega_a s}{s + \omega_a} \boldsymbol{d}_a(s) \end{aligned} \tag{11}$$

with

$$\omega_a = \frac{R_a + k_{amp} k_v k_i k_e}{L_a} \tag{12}$$

where k_a is the proportional coefficient of power amplification unit, and k_v is the amplification coefficient from the input voltage to the control current. R_a is equivalent resistance of the radial AMB unit. L_a is equivalent inductance of the radial AMB unit, and k_e is the measurement gain of current sensor.

According to the control current in Eq.(11) and the control diagram of power amplification unit in Fig. 3, the vibration displacements of rotor shaft could lead to the unbalance currents of the radial AMB units. Therefore, the researches about vibration analysis and control model of rotor shaft suspended by the radial AMB units are critical to improve the suspension stability and control performances of the MSB.

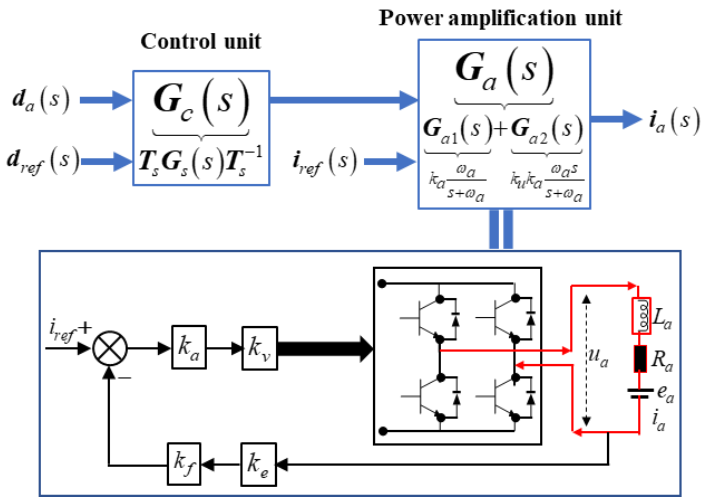

Fig. 3. The control unit and power amplification unit of the radial AMB unit.

2.3 Unbalance Vibration Models of Rotor Shaft in MSB

The mismatch errors between the inertial principal axis and the geometrical principal axis could cause the unbalance vibration of the rotor shaft in the MSB. According to the coordinate definitions of the rotor shaft in Fig. 2, the static unbalance with amplitude ε_s and phase ψ_s is used to indicate the translational vibration. The dynamic unbalance of the rotor shaft with amplitude ε_d and phase ψ_d is used to present the torsional vibration. The unbalance vibration of the rotor shaft on four-DOFs can be written as

$$\Delta \boldsymbol{d} = \boldsymbol{d}_i - \boldsymbol{d}_g = \begin{bmatrix} \varepsilon_s \cos(\Omega t + \psi_s) \\ \varepsilon_d \sin(\Omega t + \psi_d) \\ \varepsilon_s \sin(\Omega t + \psi_s) \\ -\varepsilon_d \cos(\Omega t + \psi_d) \end{bmatrix} \tag{13}$$

Substituting Eqs. (10), (11) and (13) into Eq. (8), the dynamic model of the rotor shaft is rewritten as

$$\left(\boldsymbol{M}s^2 + \boldsymbol{G}s\right)\left[\boldsymbol{d}_g(s) + \Delta \boldsymbol{d}(s)\right] = -k_i\left[\boldsymbol{T}_f \boldsymbol{T}_s \boldsymbol{G}_{a1}(s)\boldsymbol{G}_s(s) + \boldsymbol{T}_f \boldsymbol{T}_f^T \boldsymbol{G}_{a2}(s)\right]\boldsymbol{d}_g(s) + k_d \boldsymbol{T}_f \boldsymbol{T}_f^T \boldsymbol{d}_g(s) \tag{14}$$

In order to analyze the unbalance vibration of the rotor shaft on four DOFs, the complex factor j is used to decouple the four-DOFs dynamic model in Eq. (14). Furthermore, substituting $\boldsymbol{M}$ and $\boldsymbol{G}$ in Eq.(2), $\boldsymbol{T}_f$ and $\boldsymbol{T}_s$ in Eq.(4) and (5) into (14), the unbalance vibration models of rotor shaft could then be decoupled to the translational vibration and the torsional vibration written respectively as

$$f(s) = f_x(s) + f_y(s)\boldsymbol{j} = 2\left[k_d - k_i k_s \boldsymbol{G}_{a1}(s)\boldsymbol{G}_s(s) - k_i k_u s \boldsymbol{G}_{a1}(s)\right] r_g(s) \tag{15}$$

$$p(s) = p_\alpha(s) + p_\beta(s)\boldsymbol{j} = 2l_a\left[k_d l_a - k_i k_s l_b \boldsymbol{G}_{a1}(s)\boldsymbol{G}_s(s) - k_i k_u l_a s \boldsymbol{G}_{a1}(s)\right]\theta_g(s) \tag{16}$$

The four-DOFs displacement terms of rotor shaft could be expressed as

$$\begin{cases} r_g(s) = x_g(s) + y_g(s)\, j \\ \theta_g(s) = \alpha_g(s) + \beta_g(s)\, j \end{cases} \tag{17}$$

Therefore, the unbalance vibrations of rotor shaft on four-DOFs in the MSB could be investigated in the following section.

2.4 Unbalance Vibration Analysis of MSB

The control function $\boldsymbol{G}_s(s)$ of the radial AMB unit could not affect the vibration behavior of the rotor in theory, so the proportional-integral-derivative (PID) model with the proportional coefficient K_P, the integration coefficient K_I and the derivative coefficient K_D is used to analyze the vibration characteristics of rotor shaft in the MSB.

For the translational vibration along radial axis, Eq. (15) could be expressed as

$$m\ddot{r}_g - m\varepsilon_s\Omega^2 e^{j(\Omega t+\psi_s)} = 2k_d r_g - 2k_{ivs}\frac{\omega_a}{s+\omega_a}\left[K_P r_g + \left(K_D + \frac{k_u}{k_s}\right)\dot{r}_g + K_I\int r_g dt\right] \tag{18}$$

where the power coefficient of radial AMB unit is defined as $k_{ivs}= k_i k_v k_s$.

Since the equivalent EMF of radial AMB unit is smaller than 0.002 which maybe neglected, the translation vibration of rotor shaft in (18) could be simplified as

$$m\ddot{r}_g - m\varepsilon_s\Omega^2 e^{j(\Omega t+\psi_s)} = 2k_d r_g - 2k_{ivs}\frac{\omega_a}{s+\omega_a}\left[K_P r_g + K_D\dot{r}_g + K_I\int r_g dt\right] \tag{19}$$

By defining the vibration term $r_g = \varepsilon_{sg}e^{j(\Omega t+\psi_{sg})}$, the amplitude and phase of the translational vibration could be derived using Eq. (19) and written as

$$\begin{cases} \varepsilon_{sg} = \dfrac{m\Omega^2\sqrt{\omega_a^2+\Omega^2}\,\varepsilon_s}{\sqrt{\left(2K_P k_{ivs}\omega_a - m\omega_a\Omega^2 - 2k_d\omega_a\right)^2 + \left(2K_D k_{ivs}\omega_a\Omega - 2K_I\dfrac{1}{\Omega}mk_{ivs}\omega_a - m\Omega^3 - 2k_d\Omega\right)^2}} \\ \psi_{sg} = \psi_s + \tan^{-1}\left(\dfrac{\Omega}{\omega_a}\right) - \tan^{-1}\left(\dfrac{2K_D k_{ivs}\omega_a\Omega - 2K_I\dfrac{1}{\Omega}mk_{ivs}\omega_a - m\Omega^3 - 2k_d\Omega}{2K_P k_{ivs}\omega_a - m\omega_a\Omega^2 - 2k_d\omega_a}\right) \end{cases} \tag{20}$$

The torsional vibration using Eq. (16) could be derived and written as

$$J_e\ddot{\theta}_g - J_p\Omega\dot{\theta}_g j - \left(J_e - J_p\right)\varepsilon_d\Omega^2 e^{j(\Omega t+\psi_d)} = 2k_d l_a^2\dot{\theta}_g - 2l_a l_s k_{ivs}\frac{\omega_a}{s+\omega_a}\left[K_P\theta_g + K_D\dot{\theta}_g + K_I\int\theta_g dt\right] \tag{21}$$

By defining the vibration term $\theta_g = \varepsilon_{dg}e^{j(\Omega t+\psi_{dg})}$, the amplitude and phase of the tilting vibration could be derived using Eq. (21) and written as

$$\begin{cases} \varepsilon_{dg} = \dfrac{\sqrt{\left(J_e\omega_a - J_z\omega_a\right)^2 + \left(J_e\Omega - J_p\Omega\right)^2}\,\Omega^2\varepsilon_d}{\sqrt{\left[\left(J_p - J_e\right)\omega_a\Omega^2 + 2\omega_a l_a\left(k_{ivs}l_s - k_d l_a\right)\right]^2 + \left[2l_a l_s k_{ivs}\omega_a\left(K_D\Omega - \dfrac{K_P}{\Omega}\right) - 2\Omega k_d l_a^2 + \left(J_p - J_e\right)\Omega^3\right]^2}} \\ \psi_{dg} = \psi_d + \tan^{-1}\left(\dfrac{\Omega}{\omega_a}\right) - \tan^{-1}\left[\dfrac{2l_a l_b k_{ivs}\omega_a\left(K_D\Omega - \dfrac{K_P}{\Omega}\right) - 2\Omega k_d l_a^2 + \left(J_p - J_e\right)\Omega^3}{\left(J_p - J_e\right)\omega_a\Omega^2 + 2\omega_a l_a\left(k_{ivs}l_s - k_d l_a\right)}\right] \end{cases} \tag{22}$$

The vibration displacements of rotor shaft of four-DOFs measured by the radial displacement sensors are

$$\begin{bmatrix} x_{su} \\ x_{sl} \\ y_{su} \\ y_{sl} \end{bmatrix} = \boldsymbol{T}_s \begin{bmatrix} x_g \\ \beta_g \\ y_g \\ -\alpha_g \end{bmatrix} = \boldsymbol{T}_s \begin{bmatrix} \varepsilon_{sg}\cos\left(\Omega t+\psi_{sg}\right) \\ \varepsilon_{dg}\sin\left(\Omega t+\psi_{dg}\right) \\ \varepsilon_{sg}\sin\left(\Omega t+\psi_{sg}\right) \\ -\varepsilon_{dg}\cos\left(\Omega t+\psi_{dg}\right) \end{bmatrix}$$

$$= k_s \begin{bmatrix} \left(\varepsilon_{sg}\cos\psi_{sg}+\varepsilon_{dg}l_s\sin\psi_{dg}\right)\cos\Omega t+\left(-\varepsilon_{sg}\sin\psi_{sg}+\varepsilon_{dg}l_s\cos\psi_{dg}\right)\sin\Omega t \\ \left(\varepsilon_{sg}\cos\psi_{sg}-\varepsilon_{dg}l_s\sin\psi_{dg}\right)\cos\Omega t+\left(-\varepsilon_{sg}\sin\psi_{sg}-\varepsilon_{dg}l_s\cos\psi_{dg}\right)\sin\Omega t \\ \left(\varepsilon_{sg}\cos\psi_{sg}+\varepsilon_{dg}l_s\sin\psi_{dg}\right)\cos\left(\Omega t-\frac{\pi}{2}\right)+\left(-\varepsilon_{sg}\cos\psi_{sg}+\varepsilon_{dg}l_s\sin\psi_{dg}\right)\sin\left(\Omega t-\frac{\pi}{2}\right) \\ \left(\varepsilon_{sg}\cos\psi_{sg}-\varepsilon_{dg}l_s\sin\psi_{dg}\right)\cos\left(\Omega t-\frac{\pi}{2}\right)+\left(-\varepsilon_{sg}\cos\psi_{sg}-\varepsilon_{dg}l_s\sin\psi_{dg}\right)\sin\left(\Omega t-\frac{\pi}{2}\right) \end{bmatrix} \tag{23}$$

The vibration amplitude of the rotor shaft could be written as

$$\begin{aligned} \left\|x_{su}\right\| &= \left\|y_{su}\right\| = \sqrt{2\varepsilon_{sg}^2+2\varepsilon_{dg}^2l_s^2+2\varepsilon_{sg}\varepsilon_{dg}l_s\sin\left(\psi_{dg}-\psi_{sg}\right)} \\ \left\|x_{sl}\right\| &= \left\|y_{sl}\right\| = \sqrt{2\varepsilon_{sg}^2+2\varepsilon_{dg}^2l_s^2-2\varepsilon_{sg}\varepsilon_{dg}l_s\sin\left(\psi_{dg}-\psi_{sg}\right)} \end{aligned} \tag{24}$$

According to Eq.(24), the dynamic displacements and the vibration amplitudes of the rotor shaft with four-DOFs could vary with the rotating speed, the static unbalance and the dynamic unbalance.

3 Complex-exponential Function Control of Rotor Shaft

The MSB with a disc-shape impeller would be affected by the strong gyroscopic effect at high rotating speed. Especially, the nutation of rotor shaft could lead to the phase-lag of the power amplification unit. However, the suspension damping is not enough to suppress the unbalance vibration. Based on the decoupled dynamic models in Eqs. (15) and (16), a complex-factor cross-feedback model is applied to control the unbalance vibration of the rotor shaft at high rotating speed.

In general, the complex-factor cross-feedback model is designed as follows

$$G_{cr\_c}(s) = \left(k_{hc}\frac{s}{s+\omega_{hc}} - k_{lc}\frac{\omega_{lc}}{s+\omega_{lc}}\right)j\Omega \tag{25}$$

where k_{hc} and ω_{hc} are the respective control coefficient and cutoff frequency of the high-pass filter (HPF) for suppressing the high-frequency nutation, and k_{lc} and ω_{lc} are the respective control coefficient and cutoff frequency of the low-pass filter (LPF) for suppressing the low-frequency precession.

Based on the general complex-factor cross-feedback model in Eq. (25) with consideration of the phase-lag of the unbalance rotor vibration, a complex-exponential function cross-feedback model with nutation phase θ_{he} and precession phase θ_{le} is proposed to suppress the unbalance vibration of the rotor shaft written as

$$G_{cr\_e}(s) = \left(k_{he}\frac{s}{s+\omega_{he}}e^{\theta_{he}j} - k_{le}\frac{\omega_{le}}{s+\omega_{le}}e^{\theta_{le}j}\right)\Omega \tag{26}$$

Compared to the general complex-factor cross-feedback model in Eq. (25) which can suppress only the vibration amplitude of the rotor, the proposed complex-exponential factor model in Eq. (26) could also control the unbalance vibration of the rotor caused by the phase-lag. Therefore, the phase control of unbalance vibration could be regulated by tuning the nutation control coefficient θ_{he} and the precession control coefficient θ_{le}.

The major purpose of vibration control of the MSB is to ensure rotor shaft rotates about the inertial principal axis. Using the inertial four-DOFs displacement coordinate of the rotor shaft in Section 2.2, the translational

displacement terms of the rotor shaft along radial axis is defined as $r_i=x_i+y_ij$. The translational model of the rotor shaft in Eq. (19) with the cross-feedback model can be rewritten as

$$ms^2 r_i(s) = 2\left[k_d - k_{ivs}\frac{\omega_a}{s+\omega_a}G_c(s)\right]\left[r_i(s) - d(s)\right] \tag{27}$$

The vibration dynamics of the rotor shaft along *x*-axis is chosen to analyze the translational vibration, and it is written as

$$mx_i(s)s^2 = 2\left[k_d - k_i v_s\frac{\omega_a}{s+\omega_a}G_c(s)\right]\left[x_i(s) - d_x(s)\right] \tag{28}$$

where $d_x(s) = \varepsilon_s\dfrac{s\cos\psi_s - \Omega\sin\psi_s}{s^2+\Omega^2}$.

Moreover, the torsional vibration of the rotor shaft with the displacement $\theta_i=\alpha_i+\beta_ij$ could be expressed as

$$\left(J_e s^2 - J_p\Omega js\right)\theta_i(s) = 2l_a\left\{k_d l_a - k_{ivs}\frac{\omega_a}{s+\omega_a}\left[G_c(s)+G_{cr}(s)\right]\right\}\left[\theta_i(s) - I(s)\right] \tag{29}$$

The vibration dynamics of the rotor shaft around *x*-axis can be written as

$$\begin{aligned}\frac{J_e s^2\alpha_i(s) + J_p\Omega s\beta_i(s)}{2l_a} = &\left[k_d l_a - k_{ivs}l_s\frac{\omega_a}{s+\omega_a}G_{co}(s)\right]\left[\alpha_i(s) - I_\alpha(s)\right] \\ &+k_{ivs}l_s\frac{\omega_a}{s+\omega_a}G_{si}(s)\left[\beta_i(s) - I_\beta(s)\right]\end{aligned} \tag{30}$$

where $I_\alpha(s) = \varepsilon_d\dfrac{s\cos\psi_d - \Omega\sin\psi_d}{s^2+\Omega^2}$ and $I_\beta(s) = \varepsilon_d\dfrac{s\sin\psi_d + \Omega\cos\psi_d}{s^2+\Omega^2}$.

For the normal complex-factor cross-feedback model in Eq.(25), the control functions could be expressed as

$$\begin{aligned}G_{co}(s) &= G_c(s) + \frac{k_{hc}\Omega s}{s+\omega_{hc}} \\ G_{si}(s) &= \frac{k_{hc}\Omega s}{s+\omega_{hc}}\end{aligned} \tag{31}$$

For the complex-exponential factor cross-feedback model in Eq.(26), the control functions are

$$\begin{aligned}G_{co}(s) &= G_c(s) + \frac{k_{he}\Omega s}{s+\omega_{he}}\cos\theta_{he} - \frac{k_{le}\omega_{le}\Omega}{s+\omega_{le}}\sin\theta_{le} \\ G_{si}(s) &= \frac{k_{he}\Omega s}{s+\omega_{he}}\cos\theta_{he} - \frac{k_{le}\omega_{le}\Omega}{s+\omega_{le}}\sin\theta_{le}\end{aligned} \tag{32}$$

where $G_c(s)$ is the PID control model of the radial AMB unit.

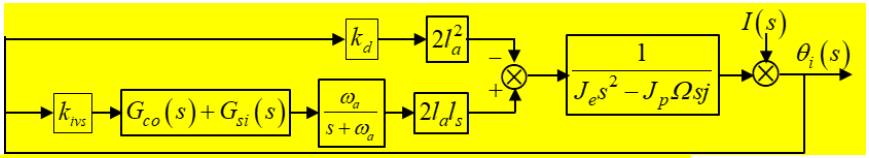

Fig. 4. The complex-exponential function cross-feedback control diagram of the rotor shaft in MSB.

Above all, the control diagram of rotor shaft using the complex-exponential function cross-feedback model is shown in Fig. 4, the complex-exponential function cross-feedback control not only suppress the vibration amplitudes of the rotor shaft caused by the unbalance terms, but it also regulate the vibration phase of the unbalanced vibration of the shaft.

4 Numerical Simulation

To verify the analysis about the unbalance vibration of the rotor shaft, numerical simulations of the unbalance vibration with the proposed complex-exponential function cross-feedback model are conducted. The static unbalance vibration amplitude and phase of the rotor shaft are chosen as ε_s=0.02 mm and ψ_s=5 rad, and the dynamic unbalance vibration are assumed to be ε_d=0.02 mm and ψ_d=5 rad. In order to ensure the simulation consistent with the actual experiment, and the K_P and K_D in the PID model are not too small values causing instability of the control system, the parameters of the PID model used in the simulation and experiment are chosen as K_P=2.2 and K_D=0.8, respectively. Moreover, too big value of K_I may also cause the control model to become unstable. Therefore, the K_I in the simulation and experiment is chosen as K_I=0.02.

4.1 Unbalance Vibration of Rotor Shaft in MSB

Firstly, the relationship between the vibration amplitude and the rotating speed is shown in Fig. 5(a) for the analysis of the unbalance vibration (expressed in Eq. (20)) caused by the static unbalance terms. The rotating speed of the MSB is increased until the vibration displacement of the rotor shaft caused by the static unbalance becomes the maximum value of 0.02 mm. This maximum value of static unbalance is consistent with the analysis result from Eq. (20). The relationship between the vibration phase and the rotating speed is shown in Fig. 5(b), and the vibration phase reaches to the defined value of 5 rad.

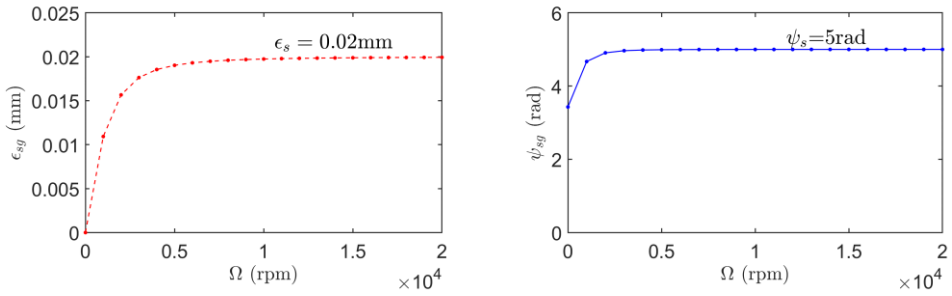

(a) (b)

Fig. 5. The unbalance vibration caused by the static unbalance of the rotor shaft, (a) the relationship between the vibration amplitude and the rotating speed, (b) the relationship between the vibration phase and the rotating speed.

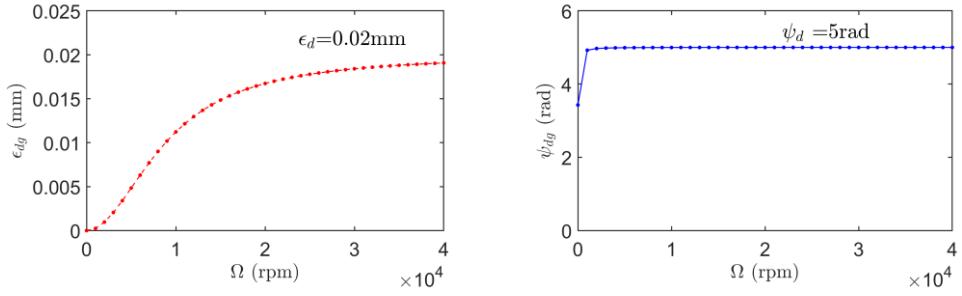

(a) (b)

Fig. 6. The unbalance vibration caused by the dynamic unbalance of rotor shaft, (a) the relationship between the vibration amplitude and the rotating speed, (b) the relationship between the vibration phase and the rotating speed.

Moreover, the vibration behavior of the rotor shaft as expressed in Eq. (22) caused by the dynamic unbalance terms is simulated. The vibration amplitude and phase of the rotor shaft with different rotating speeds are plotted in Fig. 6. In Fig. 6(a), the vibration amplitude increases with the rotating speed and approaches to the reference

value when the rotating speed of the rotor shaft is infinite. In Fig. 6(b), the vibration phase is close to the defined value when the rotating speed of rotor shaft approaches to the threshold value.

Therefore, the vibration behavior of the rotor shaft caused by the static unbalance and the dynamic unbalance can be stated as

$$\begin{aligned} &\textit{static unblance}: \quad \lim_{\Omega\to\infty}\varepsilon_{sg}=\varepsilon_s, \text{ and } \lim_{\Omega\to\infty}\psi_{sg}=\psi_s \\ &\textit{dynamic unblance}: \quad \lim_{\Omega\to\infty}\varepsilon_{dg}=\varepsilon_d, \text{ and } \lim_{\Omega\to\infty}\psi_{dg}=\psi_d \end{aligned} \tag{33}$$

The vibration amplitudes of the rotor shaft in consideration of the static unbalance and the dynamic unbalance according to Eq. (24) are plotted in Fig. 7. With different amplitudes of static unbalance and dynamic unbalance, the relationship between the vibration amplitude and the rotating speed is presented in Fig. 7(a). The vibration displacement (plotted by the red line) would reach to 0.018 mm with the rotating speed when the amplitude of static unbalance ε_s=0.01 mm and ε_d=0.02 mm, and it is increased to 0.03 mm when the amplitude (plotted by the green line) of static unbalance ε_s=0.02 mm and ε_d=0.02 mm. Moreover, the relationship between the vibration displacement and the rotating speed with different phases of the static unbalance and the dynamic unbalance is indicated in Fig. 7(b). When the respective phases of the static unbalance and the dynamic unbalance are ψ_s=0 rad and ψ_d=5 rad, the vibration displacement could be increased to a constant value about 0.025 mm as marked by the red line. The dynamic displacement is increased to 0.035 mm when ψ_s=5 rad and ψ_d=0 rad. Therefore, the amplitude of the static unbalance could intensify the vibration displacement of the rotor shaft with increasing rotating speed, and the increase of phase angle of the dynamic unbalance could mitigate the vibration displacement.

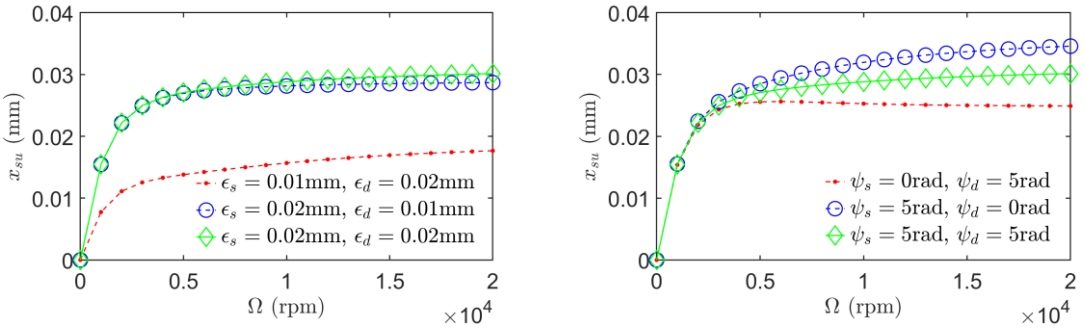

(a) (b)

Fig. 7. The vibration amplitudes of rotor shaft with the static unbalance and the dynamic unbalance, (a) the relationship between the vibration amplitude and the rotating speed with different unbalance terms, (b) the relationship between the vibration amplitude and the rotating speed with different phase terms.

4.2 Vibration Analysis of Rotor Shaft in MSB

To analyze the dynamic performances of the rotor shaft established based on the complex-factor cross-feedback model, the root loci of the model is calculated and plotted in Fig. 8 and Fig. 9 when the rotational frequency is increased from 40 Hz to 400 Hz.

Firstly, the root loci of the rotor shaft's dynamic model with different cutoff frequencies ω_{lc} and ω_{hc} are shown in Fig. 8. The root locus of the dynamic model with $\omega_{lc}=80\pi$ and $\omega_{hc}=400\pi$ is shown by the blue crosses. The root locus with $\omega_{lc}=160\pi$ and $\omega_{hc}=400\pi$ is plotted by the red circles, and the root locus at $\omega_{lc}=160\pi$ and $\omega_{hc}=800\pi$ is marked by the green stars. The detailed root loci of rotor shaft's nutation and precession are zoomed

in and shown in Fig. 8(b). The nutation frequency increases with the rotating speed, and the root locus of the nutation gets closer to the right half plane (RHP) when the cutoff frequency ω_{hc} of the HPF is reduced from 800π to 400π. Therefore, a higher cutoff frequency of the HPF could improve the stability of nutation of the rotor shaft. For the precession of rotor shaft, the precession frequency decreases with the rotating frequency, and the root locus of precession gets closer to the RHP when the cutoff frequency ω_{lc} of the LPF is reduced from 160π to 80π. Therefore, a lower cutoff frequency of the LPF could improve the precession stability of the rotor shaft.

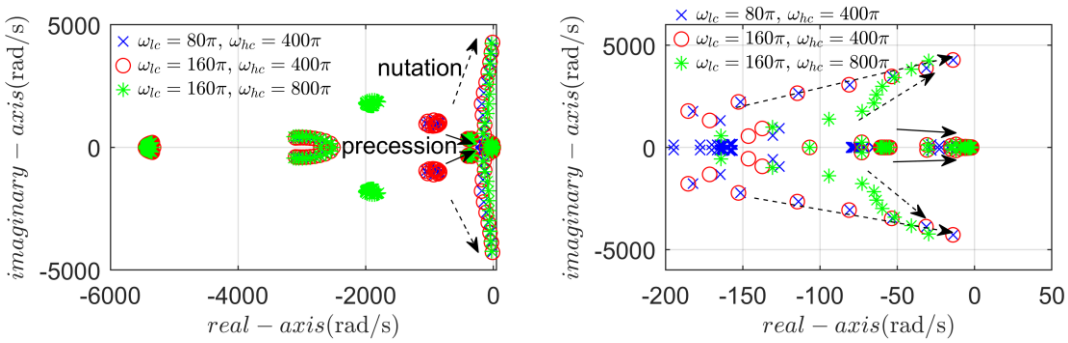

(a) (b)

Fig. 8. The root loci of rotor shaft's dynamic model with different cutoff frequencies of complex-factor cross-feedback model, (a) the whole root locus of dynamic model, (b) the part root locus of dynamic model.

Moreover, the root loci of the rotor shaft's dynamic model with different control parameters k_{lc} and k_{hc} of the LPF and the HPF are plotted in Fig. 9. The root locus of the dynamic model with k_{lc}=0.1 and k_{hc}=1 is shown by the blue crosses. The root locus with k_{lc}=0.3 and k_{hc}=1 is plotted by the red circles, and the root locus at k_{lc}=0.3 and k_{hc}=3 is marked by the green stars. In detail, for the nutation of the rotor shaft, the root locus of the nutation could be far away from the RHP when the control coefficient k_{hc} of the HPF is increased from 1 to 3. Therefore, the stability of the nutation could be enhanced by increasing the control coefficient k_{hc}. In addition, for the precession of the rotor shaft, when the control coefficient k_{lc} of the LPF is increased from 0.1 to 0.3, the root locus of precession would move farther away from the RHP. Therefore, the stability of the precession can be improved by increasing the control coefficient k_{lc} of the LPF.

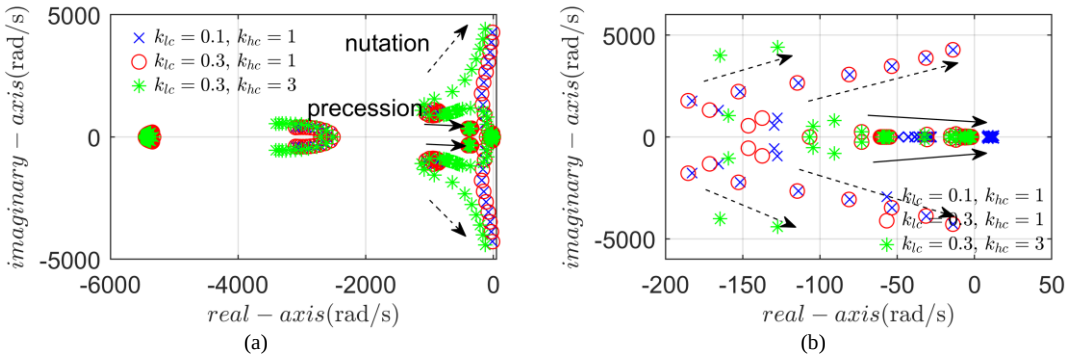

(a) (b)

Fig. 9. The root loci of rotor shaft's dynamic model with different gains of the complex-factor cross-feedback model, (a) the whole root loci of the dynamic model, (b) the detailed root loci of the dynamic model.

Therefore, the vibration stability of the rotor shaft in the MSB could be regulated by tuning the cutoff frequencies and control coefficients of the LPF and the HPF.

Furthermore, in order to verify the effectiveness of the complex-exponential function cross-feedback model, the root loci of rotor shaft with the complex-exponential function cross-feedback model are shown in Fig. 10 and Fig. 11. The root loci of the nutation and precession with different values of control coefficient θ_{he} are respectively plotted in Fig. 10(a) and 10(b). As shown by the red crosses, the root locus of nutation is far away from the RHP when the nutation control coefficient θ_{he} is increased from 0 to 2, and then it moves closer to the RHP if θ_{he} is changed from 2 to 4. Similar effect to the precession is also observed in Fig. 10(b). Therefore, an appropriate value of the nutation control coefficient θ_{he} should be used in order improve both the nutation and precession stabilities.

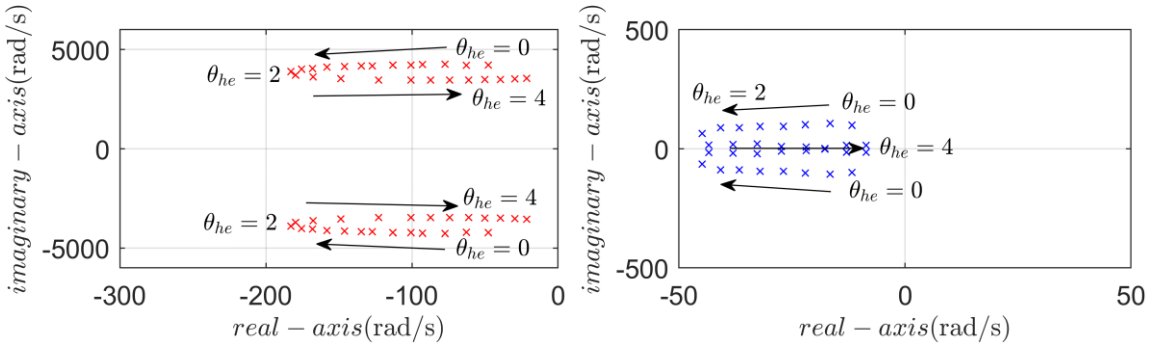

(a) (b)

Fig. 10. The root loci of rotor shaft's dynamic model with different high-pass frequencies of the complex-exponential cross-feedback model, (a) the root loci of the rotor shaft's nutation, (b) the root loci of the rotor shaft's precession.

As illustrated in Fig. 11(a), the root locus of the nutation shows only a small change from its initial value when the control coefficient θ_{le} of the precession is increased from 0 to 3. Therefore, the control coefficient θ_{le} of the precession has little effect on the nutation. Moreover, the root loci of the precession with different coefficients of θ_{le} are shown in Fig. 11(b). The root locus is far away from the RHP when the value of θ_{le} is increased from 0 to 1, but it moves to the RHP when the value of θ_{le} is increased to 3. As a result, a proper selected value of θ_{le} could improve the stability of the precession, but it has little effect to the stability of the nutation.

Therefore, the selection of the nutation control coefficient θ_{he} and the precession control coefficient θ_{le} could refer to the following flowchart in Fig.12. Firstly, the solutions of the rating angles are obtained to analyze the root locus of the nutation and the precession. The root locus of nutation is moved far away from the RHP by adjusting the nutation control coefficient and the precession control coefficient. Finally, a comprehensive analysis of the nutation and the precession is carried out, and the nutation control coefficient and the precession control coefficient could be fine tuned to get the best control performance.

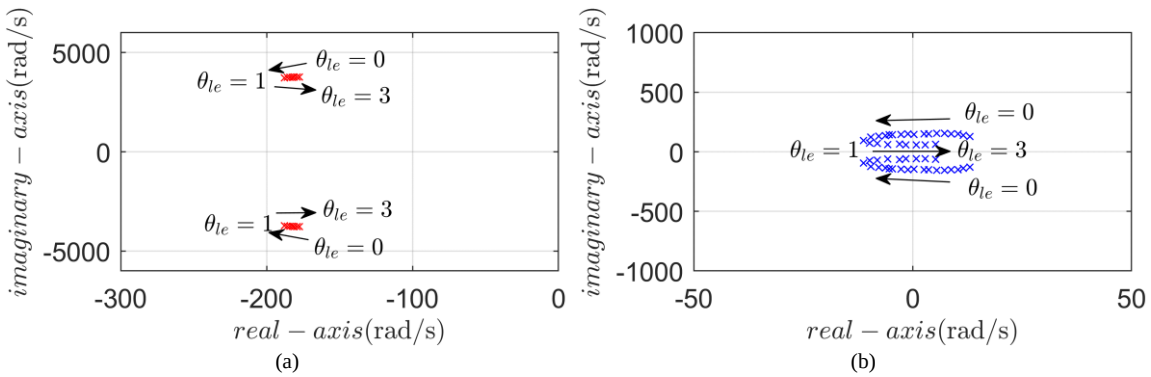

(a) (b)

Fig. 11. The root loci of rotor shaft's dynamic model with different low-pass frequencies of the complex-exponential cross-feedback model, (a) the root loci of the rotor shaft's nutation, (b) the root loci of the rotor shaft's precession.

Flowchart selection of nutation coefficient θ_{he} and precession coefficient θ_{le}	
Step 1 I, solve θ_i in Eq.(29) → distributions of α_i and β_i	▸ analyse root locus of nutation and precession
Step 2 II, ① root locus of nutation is closer to RHP → increase nutation coefficient θ_{he} III, ② root locus of nutation is closer to RHP → reduce nutation coefficient θ_{he} IV, return nutation coefficient θ_{he}	▸determine nutation coefficient θ_{he}
Step 3 V, ① root locus of precession is closer to RHP → increase nutation coefficient θ_{le} VI, ② root locus of precession is closer to RHP → reduce precession coefficient θ_{le} IV, return precession coefficient θ_{le}	▸determine precession coefficient θ_{le}
Step 4 VII, comprehensive analysis of root locus of nutation and precession → tune nutation coefficient θ_{he} and precession coefficient θ_{le}	▸tune nutation coefficient θ_{he} and precession coefficient θ_{le}

Fig. 12. Selection of the nutation control coefficient θ_{he} and the precession control coefficient θ_{le}.

4.3 Vibration Control of Rotor Shaft in MSB

To analyze and compare the control performances of the rotor shaft with different cross-feedback models, the radial displacements of the rotor shaft with the cross-feedback model at rotating speed 200 Hz are plotted in Fig. 13. For the dynamic displacements of the rotor shaft (plotted by the red line) with the complex-factor cross-feedback model, the maximum vibration displacement is about 0.21 mm, and the settling time to the steady-state value is 0.6 s. The cross-feedback model is then switched to the complex-exponential function cross-feedback model and the radial displacements of the rotor shaft are shown by the red line in Fig. 13. The maximum value of vibration displacement is 0.099 mm, and the settling time is 0.1 s. Therefore, the vibration amplitudes and the settling time of the rotor shaft are both reduced by using the proposed complex-exponential function cross-feedback model.

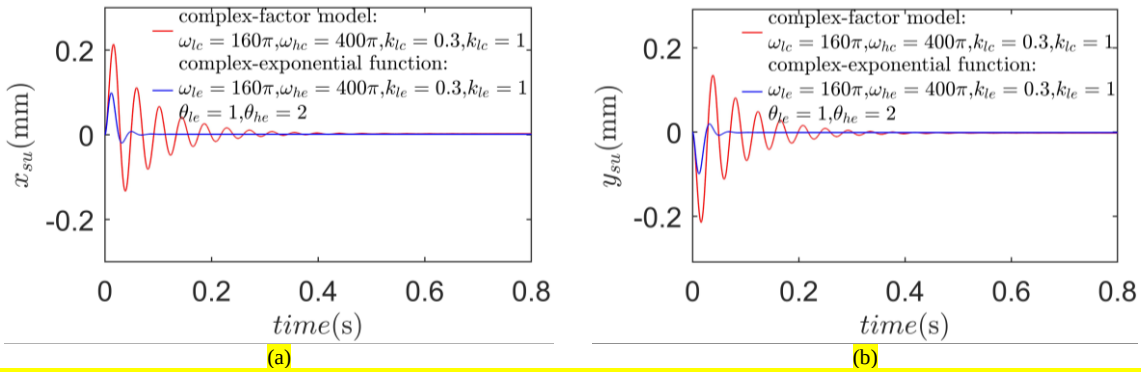

(a) (b)

Fig. 13. The radial displacements of rotor shaft using different cross-feedback control models, (a) the radial displacement x_{su} of the rotor shaft, (b) the radial displacement y_{su} of the rotor shaft.

5 Experiments

5.1 Experimental System

The vibration experiments are conducted on the MSB in Fig. 14. The vibration displacements of rotor shaft with four DOFs are timely recorded by the eddy-current displacement sensors measured at the upper-end and lower-end of the stator, and then the displacement signals are fed back to the control system of the radial AMB units through the data acquisition system (DAQ). The high-performance main control unit (MCU) using a DSP chip and a FPGA chip executes the program codes based on the displacement feedback of the rotor shaft, and then the control signal is outputted to drive the electromagnetic windings of the radial AMB units. The vibration of the rotor shaft is suppressed by the active control program of the radial AMB units. Moreover, a PMSM is used to regulate the rotating speed of rotor shaft, and experimental tests are carried out at two rotating speeds of the rotor at 600 rpm and 24000 rpm. The related parameters of the MSB are listed in TABLE I. For the rotor shaft, the mass is 26 kg. The equatorial moment of inertial is 0.13 kgm^2, and the polar moment of inertia is 0.06 kgm^2. For the radial AMB unit, the current stiffness is 606 N/A, and the displacement stiffness is -1500 N/mm. For the MCU and DAQ, the sensitivity of radial eddy-current displacement sensor is 9 V/mm. For power amplification unit, the amplification coefficient is 0.2 A/V, and the sampling frequency is 10 kHz.

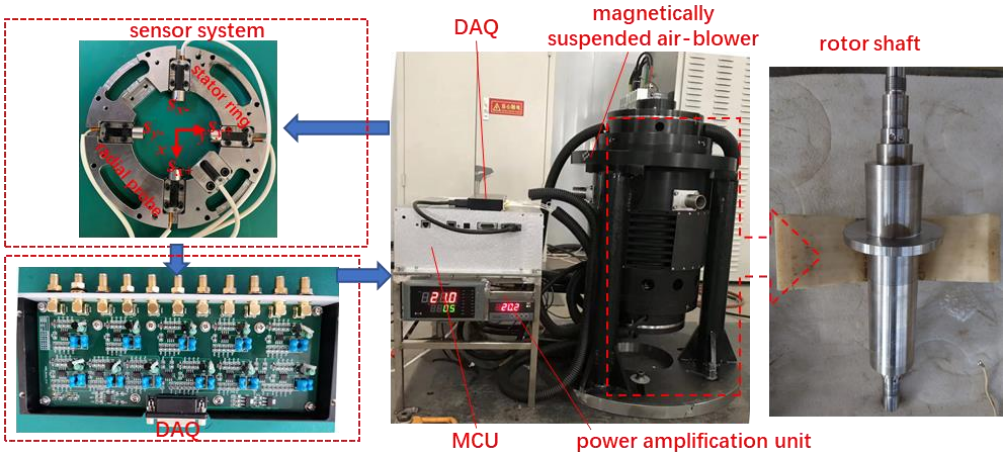

Fig. 14. The experimental setup of the MSB.

TABLE I. System parameters of the MSB

Symbol	Quantity	Value
m	mass of rotor shaft	26 kg
J_e	equatorial moment of inertia of rotor shaft	0.13 kgm^2
J_p	polar moment of inertia of rotor shaft	0.06 kgm^2
k_i	current stiffness of radial AMB unit	606 N/A
k_d	displacement stiffness of radial AMB unit	-1500 N/mm
k_s	sensitivity coefficient of radial eddy-current sensor	9 V/mm
k_v	amplification coefficient of power system	0.2 A/V

5.2 Stable Suspension of Rotor Shaft in MSB

The stable suspension is the guarantee of the active vibration control of rotor shaft in the MSB, and the suspension trajectories of rotor shaft from initial random positions to steady-state positions are plotted in Fig. 15. The blue lines indicate the suspension traces of rotor shaft at the upper-end, and the red lines show the suspension

traces at the lower-end. The initial positions (x_{su}=0.31 mm, y_{su}=0.34 mm, x_{sl}=-0.32 mm, y_{sl}=0.33 mm) of rotor shaft located on the protective mechanical bearings are random values. The rotor shaft is then levitated to the stable equilibrium positions (x_{su}=0 mm, y_{su}=0 mm, x_{sl}=0 mm, y_{sl}=0 mm) by the radial AMB units. In addition, the suspension process of rotor shaft are indicated by the axis orbit in Fig. 15(b). The axis orbit is suspended to the center-position after the rotor shaft is stably suspended at the radial equilibrium position.

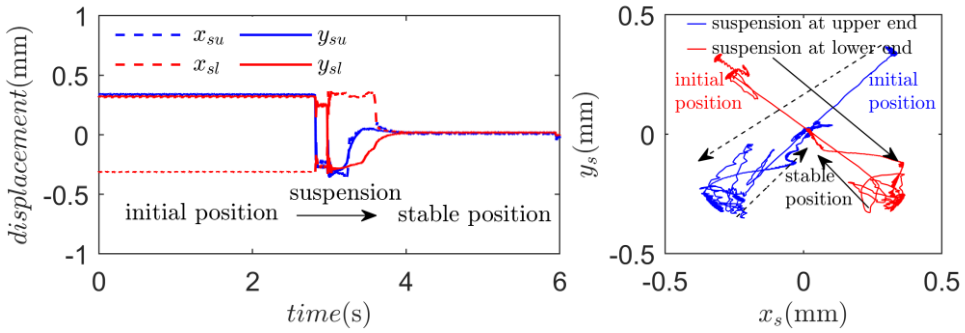

(a) (b)

Fig. 15. The suspension trajectories of rotor shaft on radial four-DOFs, (a) the four-DOFs dynamic displacements of the rotor shaft, (b) the axis orbits of the rotor shaft at the lower and upper ends.

5.3 Unbalance vibration of Rotor Shaft in MSB

To analyze the vibration characteristics of the MSB, the dynamic displacements and power spectra of the rotor shaft at different rotating speeds (600 rpm and 24000 rpm) are analyzed. Firstly, the radial displacements of rotor shaft at 600 rpm are shown in Fig. 16(a) with maximum peak-peak value of dynamic displacement 0.21 mm. The power spectrum of dynamic displacements at 600 rpm is plotted in Fig. 16(b), and the power spectrum density (PSD) is used to evaluate the vibration magnitude. The PSD of the low frequency precession is 0.012 when the rotating speed is 600 rpm. The PSD of the rotor shaft's synchronous vibration is about 0.013, and PSD of the high frequency nutation is 0.005. Therefore, the precession could lead to greater influence on the stability of the rotor shaft than the nutation.

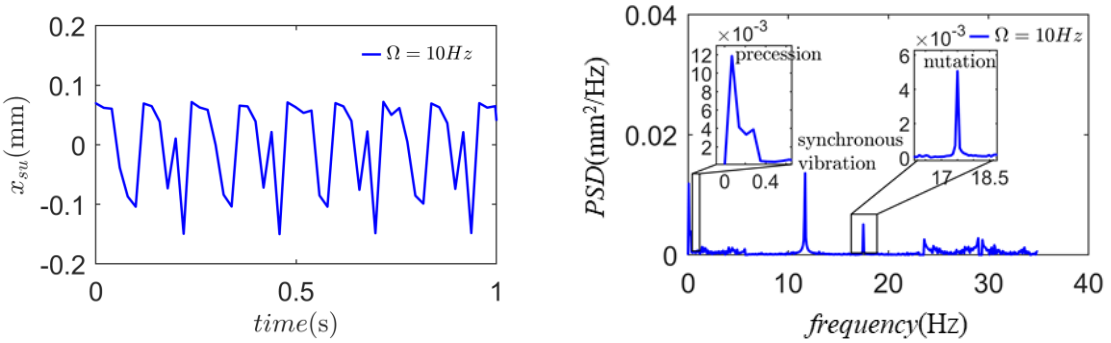

(a) (b)

Fig. 16. The vibration analysis of the rotor shaft at 600 rpm, (a) the dynamic displacements of the rotor shaft in *x*-axis, (b) the PSD of dynamic displacement.

The dynamic displacements in *x*-axis of the rotor shaft at 24000 rpm are plotted in Fig. 17(a). The peak-peak value of dynamic displacements is 0.26 mm. The power spectrum of the dynamic displacements is illustrated in Fig. 17(a). The PSD (unit is mm^2/Hz) of the low-frequency precession at 10 Hz is 0.014. The PSD of synchronous vibration at 400 Hz is 0.07, and the PSD of the high-frequency nutation at 620 Hz is 0.02. As a result, the

synchronous vibration and the nutation become more serious with the increase of rotating speed, and therefore the suppression of the nutation of rotor shaft is important to the suspension stability of the MSB.

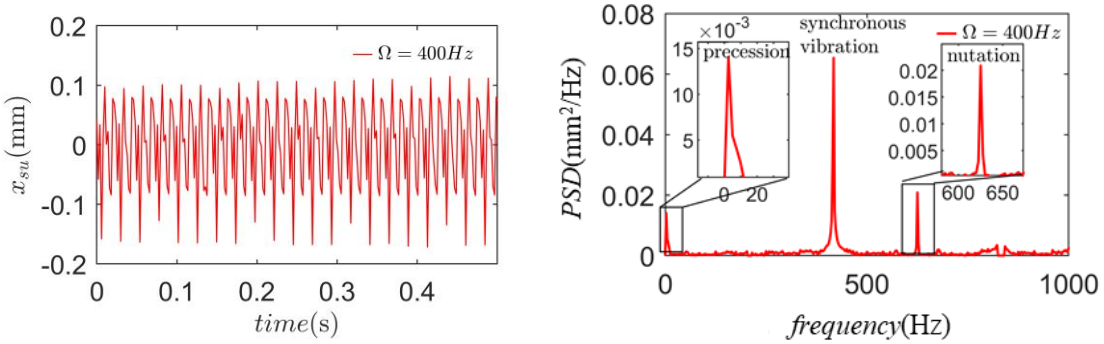

Fig. 17. The vibration analysis of the rotor shaft at 24000 rpm rotating speed, (a) the dynamic displacements of the rotor shaft in *x*-axis, (b) the PSD of dynamic displacement.

5.4 Complex-factor Cross-feedback Model of Rotor Shaft in MSB

Based on the above analysis and experiment about the vibration characteristics of rotor shaft in the MSB, the synchronous vibration and the high-frequency nutation at high rotating speed show great impact to the suspension stability of the rotor shaft. Therefore, the experiments about the MSB at high rotating speed are conducted, and the experimental results are compared and analyzed. To validate the effectiveness of the complex-factor cross-feedback model and the complex-exponential function cross-feedback model on the vibration control of the MSB, the dynamic displacements of the rotor shaft at 24000 rpm using different models are measured by the eddy-current displacement sensor [31], the corresponding power spectra of the dynamic displacements are also obtained and compared.

The dynamic displacements of the rotor shaft with different cutoff frequencies of the LPF and the HPF in the complex-factor cross-feedback model are illustrated in Fig. 18(a), and the power spectra are plotted in Fig. 18(b). In the first experiment, the cutoff frequencies of the LPF and the HPF are $\omega_{lc}=80\pi$ and $\omega_{hc}=400\pi$. The measured peak-peak dynamic displacement as shown by the blue line is 0.1736 mm. The PSD of the low-frequency precession in Fig. 18(b) is 0.0023. The PSD of synchronous vibration is about 0.0514, and the PSD of the high-frequency nutation is about 0.0287. In the second experiment, the cutoff frequencies of the LPF and the HPF are $\omega_{lc}=160\pi$ and $\omega_{hc}=400\pi$ in the experiment. The measured peak-peak displacement of the rotor shaft plotted by the red line is 0.1214 mm. The PSD of the low-frequency precession is about 0.0021. The PSD of the synchronous vibration is 0.0358, and the PSD of the high-frequency nutation is 0.0207. In the third experiment, the cutoff frequencies of the LPF and the HPF are increased to $\omega_{lc}=160\pi$ and $\omega_{hc}=800\pi$. The measured peak-peak dynamic displacements as shown by the green line is reduced to 0.1034 mm. The PSD of the low-frequency precession is 0.0021. The PSD of the synchronous vibration is 0.0254, and the PSD of the high-frequency nutation is reduced to 0.0148. Based on the comparison results of the three experiments as shown in Fig. 19, the amplitude of precession is reduced by 8.7% when the cutoff frequency of the LPF is increased from 80π to 160π, and the amplitude of the nutation is reduced by 28.5%. Therefore, by using the complex-factor cross-feedback model, the precession could be suppressed by increasing the cutoff frequency of the LPF, and the nutation could be mitigated by increasing the cutoff frequency of the HPF.

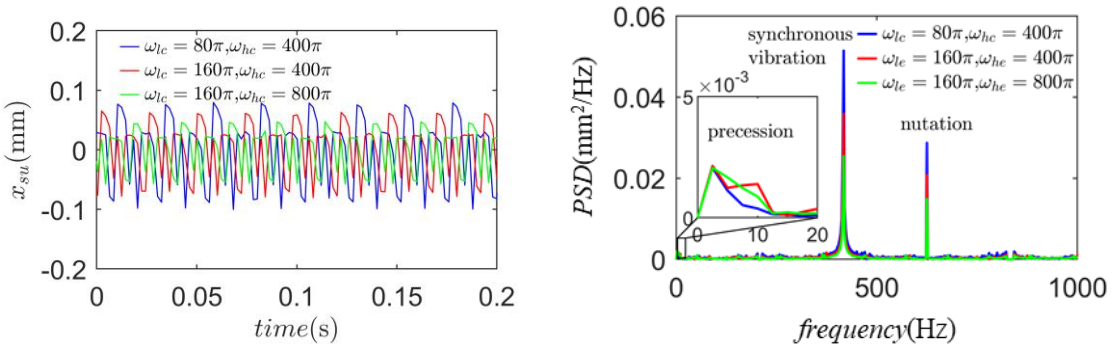

(a) (b)

Fig. 18. The displacement analysis of the rotor shaft at 24000 rpm with different cutoff frequencies of the cross-feedback model, (a) the dynamic displacements of the rotor shaft, (b) the PSD of dynamic displacements.

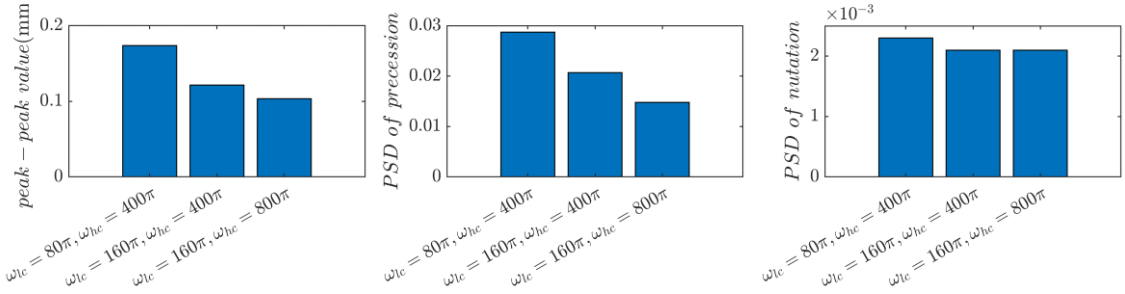

(a) (b) (c)

Fig. 19. The performance comparison of the rotor shaft at 24000 rpm with different cutoff frequencies of the cross-feedback model, (a) the dynamic displacements of the rotor shaft, (b) the PSD of precession, (c) the PSD of the nutation.

Moreover, the dynamic displacements and the power spectra of rotor shaft with different gains of the LPF and the HPF are shown in Fig. 20. In detail, the maximum displacement deflection of rotor shaft at k_{lc}=0.1 and k_{hc}=1 (shown by the blue line) is 0.1734 mm. The vibration amplitude of the low-frequency precession is 0.0039. The amplitude of the synchronous vibration is 0.0515, and the vibration amplitude of high-frequency nutation is 0.0286. When the gains of the LPF and the HPF are respectively set as k_{lc}=0.3 and k_{hc}=1, the peak-peak value of the dynamic displacements is 0.1277 mm. The PSD of the low-frequency precession is 0.0028, and the PSD of the high-frequency nutation is 0.0232. As shown by the green line, the maximum value of the dynamic displacements at k_{lc}=0.3 and k_{hc}=3 is reduced to 0.0873. The PSD of the low-frequency precession is 0.018, and the PSD of the high-frequency nutation is mitigated to 0.0179. The maximum displacement and the PSD at the three different set of gains of the LPF and the HPF are shown in Fig. 21. When the gain of the LPF is increased from 0.1 to 0.3, the dynamic displacement is reduced by 26.36%, and the PSD of the low-frequency precession is mitigated by 28.21%. When the gain of the HPF is changed from 1 to 3, the maximum value of the dynamic displacement is reduced by 31.64%, and the vibration amplitude of the high-frequency nutation is reduced by 22.84%. Therefore, the vibration magnitude of the precession could be suppressed by increasing the gain of the LPF, and vibration magnitude of the nutation could be mitigated by increasing the gain of the HPF.

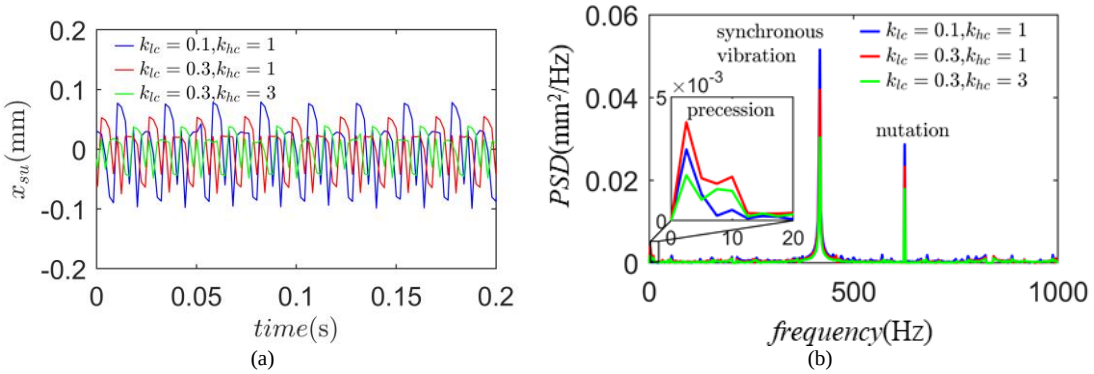

(a) (b)

Fig. 20. The displacement analysis of the rotor shaft at 24000 rpm with different gains of the cross-feedback model, (a) the dynamic displacements of the rotor shaft, (b) the PSD of dynamic displacements.

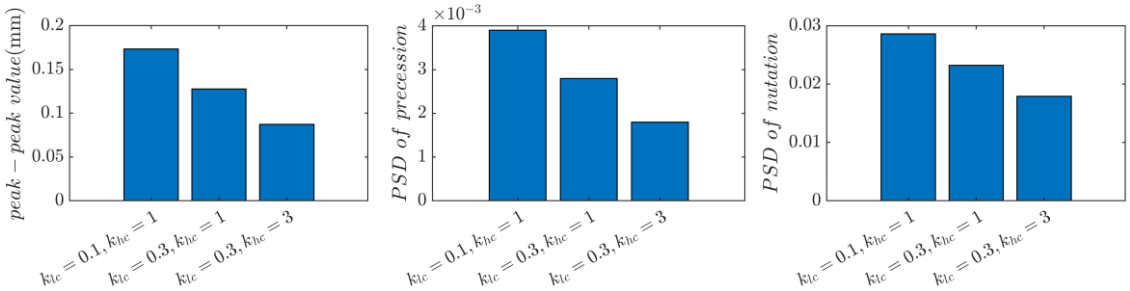

(a) (b) (c)

Fig. 21. The performance comparison of the rotor shaft at 24000 rpm with different gains of the cross-feedback model, (a) the dynamic displacements of the rotor shaft, (b) the PSD of the precession, (c) the PSD of the nutation.

5.5 Complex-exponential Function Cross-feedback Model of Rotor Shaft in MSB

A comparison between the complex-factor cross-feedback model and the complex-exponential function cross-feedback model is conducted. The measured dynamic displacements and the PSD values of the rotor shaft using the two different cross-feedback models are shown in Fig. 22. As shown by the red line, the peak-peak displacement of rotor shaft using the complex-factor cross-feedback model is 0.1223 mm. The PSD of the precession is 0.0018. The PSD of the synchronous vibration is 0.0208, and the PSD of the nutation is 0.0283. When the complex-exponential function cross-feedback model is applied to the rotor shaft in the MSB, the measured dynamic displacements of the rotor shaft is shown by the blue line. The maximum displacement deflection is 0.0663 mm. The PSD of the low-frequency precession is 0.0011. The PSD of the synchronous vibration is 0.0517, and the PSD of the high-frequency nutation is reduced to 0.0112. Consequently, the relative reduction of the maximum displacement deflection is 45.79%. The vibration amplitudes of the precession and the nutation are respectively reduced by 38.88% and 60.42%.

Moreover, the dynamic displacements of the rotor shaft in MSB when the rotating speed is regulated from 600 rpm to 24000 rpm are plotted in Fig. 23(a). For the dynamic displacements of the rotor shaft using the complex-factor cross-feedback model, the maximum value is about 0.14 mm during the acceleration process of the MSB from 600 rpm to 24000 rpm. The maximum value of the dynamic displacements with the complex-exponential function cross-feedback model is reduced to 0.05 mm. Based on the PSD of the dynamic displacement during the acceleration process in Fig. 23(b), the PSD of the dynamic displacement using the complex-exponential function cross-feedback model (blue line) is smaller than the complex-factor cross-feedback model.

Therefore, the complex-exponential function cross-feedback model is more effective than the complex-factor cross-feedback model to suppress the precession and nutation of rotor shaft in the MSB.

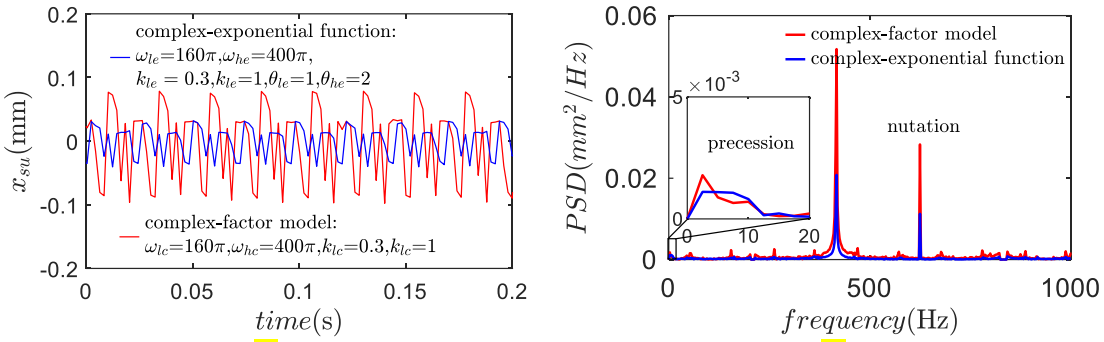

(a) (b)

Fig. 22. The displacement analysis of the rotor shaft at 24000 rpm with different cross-feedback models, (a) the dynamic displacements of the rotor shaft, (b) the PSD of dynamic displacements.

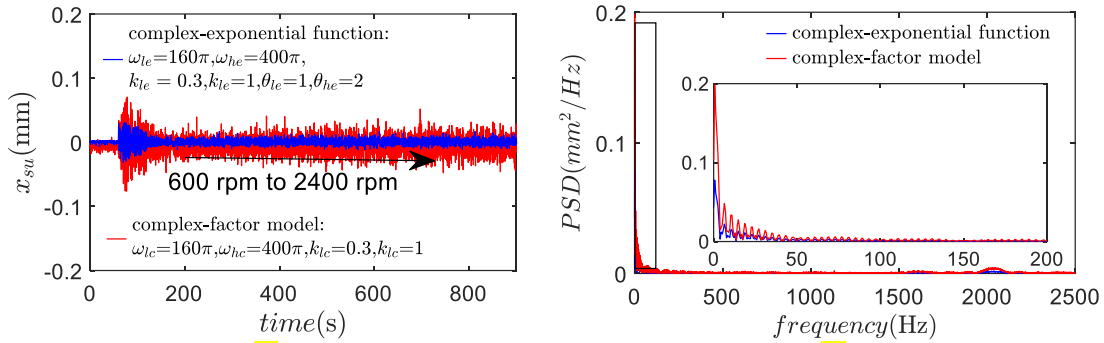

(a) (b)

Fig. 23. The displacement analysis of the rotor shaft from 600 rpm to 24000 rpm with different cross-feedback models, (a) the dynamic displacements of the rotor shaft, (b) the PSD of dynamic displacements.

TABLE II. Control performances of the rotor shaft using different control modes.

combination	displacement (peak-peak value)	PSD of precession	PSD of synchronous vibration	PSD of nutation
ω_{lc}=80π and ω_{hc}=400π	0.1736 mm	0.0023	0.0514	0.0287
ω_{lc}=160π and ω_{hc}=400π	0.1214 mm	0.0021	0.0358	0.0207
ω_{lc}=160π and ω_{hc}=800π	0.1034 mm	0.0021	0.0254	0.0148
k_{lc}=0.1 and k_{hc}=1	0.1734 mm	0.0039	0.0515	0.0286
k_{lc}=0.3 and k_{hc}=1	0.1277 mm	0.0028	0.0418	0.0232
k_{lc}=0.3 and k_{hc}=3	0.0873 mm	0.0018	0.0303	0.0179
complex-factor cross-feedback model	0.1223 mm	0.0018	0.0208	0.0283
complex-exponential function cross-feedback model	0.0663 mm	0.0011	0.0517	0.0112

6 Conclusion

The vibration characteristics and active vibration control of the rotor shaft in the MSB are investigated using the accurate dynamic models of four-DOFs. A complex-factor and complex-exponential function cross-feedback models are respectively applied in the active vibration control of the rotor shaft at high rotating speed. The vibration amplitude of rotor shaft could be affected by the rotor unbalance and rotating speed. The vibration amplitudes caused by the static unbalance and the dynamic unbalance could approach to the initially defined values by increasing the rotating speed. Experimental results indicate that the wide cutoff frequency of the LPF

in the complex-factor cross-feedback model could mitigate the precession, and the wide cutoff frequency of the HPF could suppress the amplitude of nutation. The complex-exponential function cross-feedback model can further reduce the vibration amplitude of precession of the rotor by 38.88%, and the vibration amplitude of the nutation by 60.42%. Therefore, the proposed complex-exponential function cross-feedback model could be more effective than the complex-factor function cross-feedback model in suppressing the dynamic displacement and the vibration amplitude of the rotor shaft in the MSB.

References

[1] C. Fu, J.-J. Sinou, W. Zhu, K. Lu, Y. Yang, A state-of-the-art review on uncertainty analysis of rotor systems, Mechanical Systems and Signal Processing, 183 (2023) 109619.
[2] A. Kras, P. Gardonio, Active vibration control unit with a flywheel inertial actuator, Journal of Sound and Vibration, 464 (2020) 114987.
[3] P. Varney, I. Green, Nonlinear phenomena, bifurcations, and routes to chaos in an asymmetrically supported rotor–stator contact system, Journal of Sound and Vibration, 336 (2015) 207-226.
[4] I. Virgala, P. Frankovský, M. Kenderová, Friction effect analysis of a DC motor, American Journal of Mechanical Engineering, 1 (2013) 1-5.
[5] R.S. Srinivas, R. Tiwari, C. Kannababu, Application of active magnetic bearings in flexible rotordynamic systems–A state-of-the-art review, Mechanical Systems and Signal Processing, 106 (2018) 537-572.
[6] T. Soni, A. Das, J. Dutt, Active vibration control of ship mounted flexible rotor-shaft-bearing system during seakeeping, Journal of Sound and Vibration, 467 (2020) 115046.
[7] X. Ye, X. Xu, T. Wen, B. Han, Design and optimization of repeatable locking/unlocking device for magnetically suspended control moment gyro, Acta Astronautica, 186 (2021) 24-32.
[8] R. Lungu, M. Lungu, C. Efrim, Attitude Adaptive Control of Satellites using Double-Gimbal Magnetically Suspended Control Moment Gyros, Aerospace Science and Technology, (2022) 107652.
[9] B. Xiang, H. Liu, Y. Yu, Gimbal effect of magnetically suspended flywheel with active deflection of Lorentz-force magnetic bearing, Mechanical Systems and Signal Processing, 173 (2022) 109081.
[10] M. Ahrens, L. Kucera, R. Larsonneur, Performance of a magnetically suspended flywheel energy storage device, IEEE Transactions on control systems technology, 4 (1996) 494-502.
[11] X. Li, A. Palazzolo, A review of flywheel energy storage systems: state of the art and opportunities, Journal of Energy Storage, 46 (2022) 103576.
[12] B. Xiang, X. Wang, W.O. Wong, Process control of charging and discharging of magnetically suspended flywheel energy storage system, Journal of Energy Storage, 47 (2022) 103629.
[13] G. Martynenko, Stability Analysis of Rotor Motion in Nonlinear Systems with Passive and Active Magnetic Bearings, Nonlinear Mechanics of Complex Structures, Springer, 2021, pp. 333-351.
[14] M. Hutterer, D. Wimmer, M. Schrödl, Control of magnetically levitated rotors using stabilizing effects of gyroscopes, Mechanical Systems and Signal Processing, 166 (2022) 108431.
[15] B. Xiang, W.O. Wong, Vibration characteristics analysis of magnetically suspended rotor in flywheel energy storage system, Journal of Sound and Vibration, 444 (2019) 235-247.
[16] A. Kandil, Investigation of the whirling motion and rub/impact occurrence in a 16-pole rotor active magnetic bearings system with constant stiffness, Nonlinear Dynamics, 102 (2020) 2247-2265.
[17] S.K. Kuppa, M. Lal, Dynamic behaviour analysis of coupled rotor active magnetic bearing system in the supercritical frequency range, Mechanism and Machine Theory, 152 (2020) 103915.
[18] R. Tiwari, P. Kumar, An innovative virtual trial misalignment approach for identification of unbalance, sensor and active magnetic bearing misalignment along with its stiffness parameters in a magnetically levitated flexible rotor system, Mechanical Systems and Signal Processing, 167 (2022) 108540.
[19] T. Soni, J.K. Dutt, A. Das, Dynamic behavior and stability of energy efficient electro-magnetic suspension of rotors involving time delay, Energy, 231 (2021) 120906.
[20] R. Ebrahimi, M. Ghayour, H. Mohammad Khanlo, Chaotic vibration analysis of a coaxial rotor system in active magnetic bearings and contact with auxiliary bearings, Journal of Computational and Nonlinear Dynamics, 12 (2017).
[21] M. Hutterer, D. Wimmer, M. Schrödl, Stabilization of a magnetically levitated rotor in the case of a defective radial actuator, IEEE/ASME Transactions on Mechatronics, 25 (2020) 2599-2609.
[22] B. Xiang, W. Wong, Decoupling control of magnetically suspended motor rotor with heavy self-weight and great moment of inertia based on internal model control, Journal of Vibration and Control, 28 (2022) 1591-1604.
[23] M.O. Cole, W. Fakkaew, An active magnetic bearing for thin-walled rotors: vibrational dynamics and stabilizing control, IEEE/ASME Transactions on Mechatronics, 23 (2018) 2859-2869.
[24] N. Numanoy, J. Srisertpol, Vibration reduction of an overhung rotor supported by an active magnetic bearing using a decoupling control system, Machines, 7 (2019) 73.
[25] C. Peng, J. Sun, C. Miao, J. Fang, A novel cross-feedback notch filter for synchronous vibration suppression of an MSFW with significant gyroscopic effects, IEEE Transactions on Industrial Electronics, 64 (2017) 7181-7190.
[26] Z. Jin, X. Sun, Z. Yang, S. Wang, L. Chen, K. Li, A novel four degree-of-freedoms bearingless permanent magnet machine using modified cross feedback control scheme for flywheel energy storage systems, International Journal of Applied Electromagnetics and Mechanics, 60 (2019) 379-392.
[27] G.B. Gallego, L. Rossini, T. Achtnich, D.M. Araujo, Y. Perriard, Novel Generalized Notch Filter for Harmonic Vibration Suppression in Magnetic Bearing Systems, IEEE Transactions on Industry Applications, 57 (2021) 6977-6987.

[28] J. Li, G. Liu, P. Cui, S. Zheng, Q. Chen, Synchronous vibration suppression of magnetically suspended rotor system using improved adaptive frequency estimation, IEEE Sensors Journal, 20 (2020) 11212-11220.
[29] H. Sugimoto, M. Miyoshi, A. Chiba, Axial vibration suppression by field flux regulation in two-axis actively positioned permanent magnet bearingless motors with axial position estimation, IEEE Transactions on Industry Applications, 54 (2017) 1264-1272.
[30] F. Carmo Carvalho, M.V. Fernandes de Oliveira, F.A. Lara-Molina, A.A. Cavalini Jr, V. Steffen Jr, Fuzzy robust control applied to rotor supported by active magnetic bearing, Journal of Vibration and Control, 27 (2021) 912-923.
[31] L. Zheng, W. Nie, Z. Liu, B. Xiang, Wide-range Displacement Sensor for Vibration Measurement of Magnetically Suspended Air-blower, IEEE Sensors Journal, (2022).